atoms

MDPI

Article

Single Sr Atoms in Optical Tweezer Arrays for Quantum Simulation

Veronica Giardini [1,2,†], Luca Guariento [3,4,†,‡], Andrea Fantini [2,†], Shawn Storm [2], Massimo Inguscio [1,3], Jacopo Catani [3,1], Giacomo Cappellini [3,1,‡], Vladislav Gavryusev [2,1,*] and Leonardo Fallani [2,1,3]

[1] European Laboratory for Non-Linear Spectroscopy (LENS), University of Florence, via N. Carrara 1, 50019 Sesto Fiorentino, Italy;
[2] Department of Physics and Astronomy, University of Florence, via G. Sansone 1, 50019 Sesto Fiorentino, Italy;
[3] National Institute of Optics (CNR-INO), National Research Council, via N. Carrara 1, 50019 Sesto Fiorentino, Italy;
[4] Department of Physics Ettore Pancini, University of Napoli Federico II, via Cinthia 21, 80126 Napoli, Italy
* Correspondence: vladislav.gavryusev@unifi.it
† These authors contributed equally to this work.
‡ Current address: Eniquantic S.p.A., via Ostiense 72, 00154 Roma, Italy

Abstract: We report on the realization of a platform for trapping and manipulating individual ^{88}Sr atoms in optical tweezers. A first cooling stage based on a blue shielded magneto-optical trap (MOT) operating on the $|^1S_0\rangle \to |^1P_1\rangle$ transition at 461 nm enables us to trap approximately 4×10^6 atoms at a temperature of 6.8 mK. Further cooling is achieved in a narrow-line red MOT using the $|^1S_0\rangle \to |^3P_1\rangle$ intercombination transition at 689 nm, bringing 5×10^5 atoms down to 5 µK and reaching a density of 4×10^{10} cm^{-3}. Atoms are then loaded into 813 nm tweezer arrays generated by crossed acousto-optic deflectors and tightly focused onto the atoms with a high-numerical-aperture objective. Through light-assisted collision processes we achieve the collisional blockade, which leads to single-atom occupancy with a probability of about 50%. The trapped atoms are detected via fluorescence imaging with a fidelity of 99.986(6)%, while maintaining a survival probability of 97(2)%. The release-and-recapture measurement provides a temperature of 12.92(5) µK for the atoms in the tweezers, and the ultra-high-vacuum environment ensures a vacuum lifetime higher than 7 min. These results demonstrate a robust alkaline-earth tweezer platform that combines efficient loading, cooling, and high-fidelity detection, providing the essential building blocks for scalable quantum simulation and quantum information processing with Sr atoms.

Keywords: optical tweezer; ultracold atom; quantum simulation; Sr; magneto-optical trap

PACS: 67.85.-d; 37.10.De; 37.10.Gh

check for updates

Academic Editor: Gordon W.F. Drake

Received: 2 November 2025
Revised: 28 November 2025
Accepted: 10 December 2025
Published: 19 December 2025

Citation: Giardini, V.; Guariento, L.; Fantini, A.; Storm, S.; Inguscio, M.; Catani, J.; Cappellini, G.; Gavryusev, V.; Fallani, L. Single Sr Atoms in Optical Tweezer Arrays for Quantum Simulation. *Atoms* **2026**, *14*, 1. https://doi.org/10.3390/atoms14010001

1. Introduction

Arrays of single neutral atoms trapped in optical tweezers have emerged as a versatile platform for quantum science, enabling advances in quantum simulation, quantum computation, and metrology [1–8]. These systems offer a unique combination of precise atomic control and scalability, making them ideally suited to investigate many-body quantum phenomena. Recent years have witnessed rapid progress, including demonstrations of quantum simulation with Rydberg interactions [9–12] and entangling operations between individually trapped atoms [13,14]. Alkaline-earth(-like) atoms, such as Sr and Yb, offer unique advantages for quantum science. Their narrow optical transitions enable efficient laser cooling and form the basis of state-of-the-art optical atomic clocks [15,16]. The presence of long-lived metastable states grants access to rich electronic structures and enables advanced quantum state control [17–19]. These properties make alkaline-earth(-like) atoms ideal for realizing quantum simulation, precision metrology, and quantum information platforms [20–22]. Recent developments have extended these systems to optical tweezer arrays [23–25], where narrow-line cooling, long coherence times, and strong Rydberg interactions allow for single-atom resolved control and imaging [13,26–30]. These developments establish alkaline-earth tweezer arrays as a promising setting to explore strongly correlated quantum matter, realize programmable entangling operations, and interface many-body systems with precision metrology.

Here, we present an optical tweezer platform based on individually trapped bosonic strontium (^{88}Sr) atoms. First, cold ensembles prepared via sequential blue and red magneto-optical traps (MOT) are loaded into arrays of tightly focused 813 nm tweezers. Then, light-assisted collisions ensure collisional blockade, leading to single-atom occupancy with a probability of about 50%. Fluorescence detection with a high-numerical-aperture objective enables single-atom readout with a fidelity of 99.986(6)%, while the achieved temperature of 12.92(5) µK, survival probabilities of 97(2)%, and a vacuum lifetime exceeding 400 s confirm the stability of the system. Together, these results establish a robust Sr tweezer platform [31,32] that combines efficient preparation, robust control, and high-fidelity detection, paving the way for scalable experiments on quantum simulation and quantum information processing with alkaline-earth atoms.

2. Experimental Platform

We realized a platform for trapping and manipulating single ^{88}Sr atoms in optical tweezers. The apparatus is based on a custom ultra-high vacuum (UHV) system that ensures long atomic lifetimes required for high-precision experiments. The science chamber is a fused silica glass cell providing excellent optical access, surrounded by two sets of coils. A pair of high-field coils supplies the magnetic field gradients for magneto-optical trapping as well as strong bias fields for clock-state manipulation, while six auxiliary compensation coils enable the three-dimensional control of the magnetic environment, allowing both active cancellation of stray fields and the application of tunable bias fields for state preparation. A high-numerical aperture microscope objective simultaneously generates sub-micron waist optical tweezers and collects atomic fluorescence with single-atom resolution. This configuration combines precise control over individual atoms with high-fidelity state detection. Dedicated laser systems provide cooling, optical pumping, and trapping, completing a versatile platform ideally suited for scalable quantum simulation and quantum information processing with alkaline-earth atoms.

2.1. Vacuum System

The vacuum system is designed to maintain ultra-high vacuum (UHV) conditions, which are essential for trapping and manipulating single Sr atoms [33–35]. It consists of three main sections: a commercial atomic source, a pumping chamber, and a glass cell where the optical tweezers are formed and single-atom imaging takes place, as illustrated in Figure 1a. A stable flux of Sr atoms is generated by an atomic source system (AOSense Inc., Fremont, USA), which includes a Zeeman slower as well as a 2D MOT stage that employ a permanent-magnet assembly to transversely cool and collimate the atomic beam. The slowed atoms are directed towards the science cell through a differential pumping tube, which preserves the vacuum gradient while allowing for a high flux of slowed atoms. The 2D MOT acts also as an optically controlled deflection stage that allows for switching on and off the slowed-down atom flux, which is deflected by 20° with respect to the Zeeman slower axis. Following the differential pumping tube, the atoms pass through a dedicated pumping chamber that houses an Ion–NEG combination pump (SAES Getters S.p.A., Milano, Italy, NEXTorr D500 Starcell), a Bayard–Alpert UHV gauge (Agilent Technologies Inc., Santa Clara, USA, UHV-24P), and an angle valve that provides access to an external rough pumping station. During initial pump-down, a scroll pump and turbo pump are attached through this valve, while a residual gas analyzer (Stanford Research Systems, Sunnyvale, USA, RGA200) monitors partial pressures during the bakeout procedure. The pumping chamber was designed to minimize outgassing and ensure long-term pressure stability. Downstream, the atoms enter the rectangular science cell, whose elongated planar faces maximize optical access for the laser beams required for cooling, trapping, and imaging (anti-reflection coated on the wider sides). The entire vacuum assembly is mounted on a translation stage, which provides mechanical decoupling from the rest of the apparatus and facilitates alignment and maintenance. The system was subject to an extended bakeout sequence to remove residual gases and routinely achieves base pressures below 7×10^{-12} Torr. Particular attention was devoted to material selection, sealing methods, and thermal cycling in order to suppress leaks and guarantee long-term integrity. Under these conditions, the vacuum system supports atom vacuum lifetimes compatible with long trapping and imaging sequences, as characterized in Section 3.5. This architecture thus provides the stable and collision-free environment required for high-fidelity single-atom trapping and detection.

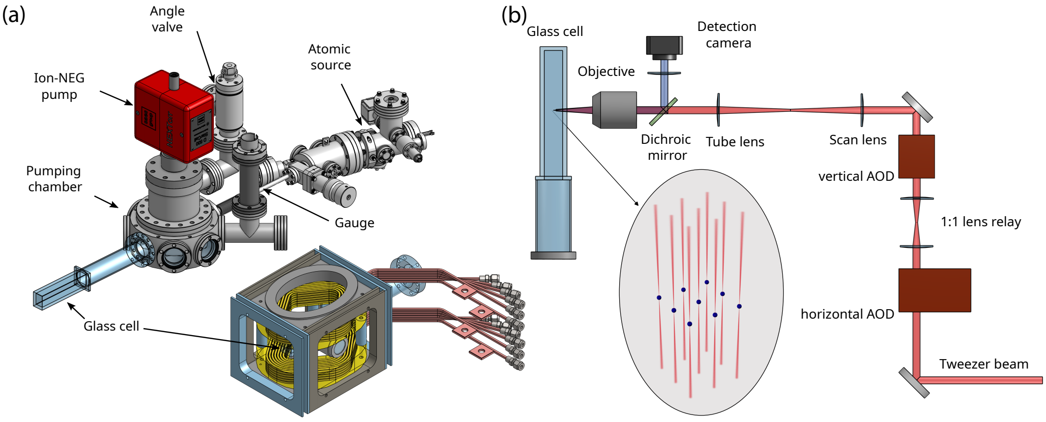

Figure 1. Overview of the experimental setup. (**a**) Vacuum system composed of a commercial atomic source, connected through a differential pumping tube to a pumping chamber which holds an ion–NEG pump, a Bayard–Alpert gauge and an angle valve. The fused silica glass science cell, where trapping and detection occur, is surrounded by two sets of magnetic coils: a pair of high-field coils providing the MOT gradient and strong bias fields for clock-state manipulation, and six smaller compensation coils that enable full three-dimensional control and active cancellation of stray fields. (**b**) Optical layout for tweezer generation and imaging. A high-power 813 nm beam passes through a pair of crossed AODs to produce an array of deflected beams. A relay telescope and a high-numerical-aperture objective (NA = 0.55) couple the angular deflection to the focal plane of the objective to form an array of spatially-displaced tightly-focused optical tweezers. The same objective collects atomic fluorescence, which is separated by a dichroic mirror and imaged onto a low-noise qCMOS detection camera for single-atom readout.

2.2. Magnetic Field Control

Two sets of coils are employed to control the magnetic environment of the experiment. The first consists of a pair of copper hollow-core water-cooled high-field coils (total resistance 60 mΩ and inductance 600 µH) capable of generating magnetic fields up to 1000 G in a Helmholtz configuration. These coils provide the strong bias fields required for excitation of the clock transition in bosonic ^{88}Sr [36,37] and can also be operated in anti-Helmholtz configuration to generate the field gradients needed for the MOTs, reaching up to 100 G cm^{-1} at the peak current of 200 A provided by the power supply (Delta Elektronika, Zierikzee, Netherlands, SM6000 30-200). In addition, three pairs of low-field compensation coils, driven by smaller power supplies (Delta Elektronika, ES150 015-10), are used to provide three-dimensional compensation of stray fields and fine adjustment of the trapping region in the red MOT.

To achieve rapid magnetic field switching, we implemented a fast discharge *snubber* circuit using a solid state electronic design [32] with time constant of $240(10)$ µs. An Insulated-Gate Bipolar Transistor (IGBT) (Semikron, Nuremberg, Germany, SKM400GAL12T4) controls the current flow in the high-field coils and is actuated by a gate driver (Semikron, SKHI 10/17R) triggered via a TTL signal. When the IGBT is turned off, the inductive energy loaded into the coils has to be dissipated and this causes a voltage surge within the circuit that can reach hundreds of volts on a sub-millisecond timescale. Voltage surge protection is provided by placing a varistor (LittleFuse, Rosemont, USA, V25S250P, conduction voltage $\geq$ 390 V) in parallel with the IGBT, and, in parallel with the coils, a branch with a diode and a 10 Ω resistor in series, to ensure safe and fast dissipation when the varistor is below threshold. An additional protective varistor (conduction voltage $\geq$ 75 V) is located in parallel with the power supply. This circuit allows a fast current decay in $240(10)$ µs that minimizes residual magnetic fields, essential for stage transitions (e.g., blue-to-red MOT as depicted in figure 2) and for precise imaging free from Zeeman shifts. As a future improvement, a custom H-bridge circuit has been designed and will soon be implemented, enabling fast switching between Helmholtz and anti-Helmholtz operation [13].

2.3. Laser Systems

The experimental setup relies on four primary laser systems that provide cooling, trapping, and coherent manipulation of individual ^{88}Sr atoms. The electronic level structure of this isotope is presented in Figure 3(a), displaying the wavelength and the decay rate of the transitions of interest. A blue laser at 461 nm (Moglabs, Carlton, Australia, ILA) addresses the broad $|^1S_0\rangle \to |^1P_1\rangle$ transition and serves multiple purposes in the experimental sequence: it provides Zeeman slowing of the atomic beam, drives the 2D MOTs, operates the first stage of the 3D MOT, and is used for fluorescence imaging. The two associated *repumping* transitions ($|^3P_0\rangle \to |^3S_1\rangle$ at 679 nm and $|^3P_2\rangle \to |^3S_1\rangle$ at 707 nm) are addressed by two tunable diode lasers (Toptica Photonics AG, Munich, Germany, DL Pro). A second stage of 3D MOT is performed with a red laser at 689 nm (MSquared, Glasgow, UK, SolsTiS-PSX-PIK), resonant with the narrow intercombination line $|^1S_0\rangle \to |^3P_1\rangle$, that is also used for in-tweezer cooling and manipulation. Optical tweezers are formed by an 8 W near-infrared laser at 813 nm (Sirah, Grevenbroich, Germany, Matisse 2 TS), delivered to the experiment table through a photonic crystal fiber (NKT Photonics, Regensdorf, Switzerland, LMA-PM-15) and operating at the magic wavelength for the $|^1S_0\rangle \to |^3P_0\rangle$ clock transition, thereby suppressing differential light shifts. In addition, ultraviolet light in the $316 - 319$ nm range is generated by frequency quadrupling a tunable infrared source (Vexlum, Tampere, Finland, VALO SF $1264 - 1278$ nm) in a two-stage fourth harmonic generation (FHG) cavity (LEOS Solutions, Rovereto, Italy), producing more than 110 mW of UV power. The wide tunability of this system will enable two complementary excitation schemes to $|nS\rangle$ Rydberg states, either via the $|^3P_0\rangle$ clock state in a two-step process [13] or through a two-photon transition from the $|^3P_1\rangle$ state [38].

Frequency stabilization is adapted to the specific requirements of each laser. The 461 nm system is locked to the spectroscopic reference provided by the $|^1S_0\rangle \to |^1P_1\rangle$ transition, while the tweezer laser at 813 nm and the two repumper lasers are stabilized using the feedback of a high-resolution wavemeter (HighFinesse, Tubinga, Germany, WS8-10, 10 MHz absolute accuracy). For the narrow-linewidth transitions, both the 689 nm and the UV lasers (through the intermediate SHG emission at $632 - 638$ nm) are stabilized to an ultra-low expansion cavity (Stable Laser Systems) with high finesse ($\approx 2.65 \times 10^5$) using Pound–Drever–Hall locking, yielding kHz linewidths and frequency stability compatible with precision control of alkaline-earth atoms.

2.4. Two-Stage Magneto-Optical Trap

To reach the temperatures and densities required for efficient atom loading into the optical tweezers we employ a two-stage MOT, which provides sufficiently low temperatures and high atomic densities [39–42]. The atomic beam is first slowed and transversely cooled using a Zeeman slower and a two-dimensional MOT stage inside the AOSense assembly, providing a continuous flux of atoms with an average speed of $40\,\mathrm{m\,s^{-1}}$. These atoms are then captured in a two-stage, three-dimensional MOT.

The first *blue* MOT operates on the broad $|^1\mathrm{S}_0\rangle \to |^1\mathrm{P}_1\rangle$ transition at 461 nm ($\Gamma/2\pi = 32\,\mathrm{MHz}$). During this stage, two repumping lasers at 679 nm and 707 nm, addressing the $|^3\mathrm{P}_0\rangle \to |^3\mathrm{S}_1\rangle$ and $|^3\mathrm{P}_2\rangle \to |^3\mathrm{S}_1\rangle$ transitions, respectively, prevent population trapping in dark states [43–45], allowing efficient capture of atoms and cooling to a few mK, while increasing the atom number by approximately an order of magnitude.

However, density-dependent losses and radiation trapping in this stage limit the achievable atom number [46]. To mitigate these effects, we apply a weak beam resonant with the fully cycling narrow intercombination line $|^1\mathrm{S}_0\rangle \to |^3\mathrm{P}_1\rangle$ at 689 nm ($\Gamma/2\pi = 7.6\,\mathrm{kHz}$) that transfers atoms into a long-lived state, effectively reducing reabsorption and inelastic collisions in the blue MOT volume, such that it acts as a loss *shield*. As demonstrated in recent studies [46], this mechanism enhances the steady-state atom number up to a factor of 2 by providing an auxiliary reservoir that continuously replenishes the blue MOT, while suppressing light-assisted losses. As the 689 nm laser system is already employed in the second MOT stage, the inclusion of the *shielding* beam does not add experimental complexity.

Considering that temperatures and densities achieved in the first MOT stage are insufficient for direct tweezer loading, a second *red* cooling stage is implemented using the narrow intercombination line $|^1\mathrm{S}_0\rangle \to |^3\mathrm{P}_1\rangle$. Since the linewidths of the blue and red transitions differ by more than three orders of magnitude, the radiation pressure force from the narrow-line red MOT is too weak to efficiently capture and cool atoms moving at velocities of order $\sim \mathrm{m\,s^{-1}}$, as is typical for atoms in the blue MOT. To overcome this limitation, we perform an intermediate *multi-frequency broadband* (BB) red MOT stage in which the 689 nm light is spectrally broadened by modulating, with an arbitrary waveform generator (AWG) (Siglent Technologies, Shenzhen, China, SDG6022X), the radio-frequency (RF) signal that drives an acousto-optical modulator (AOM) [34,47]. This loading phase increases the effective scattering rate over a wider velocity range, which enables capturing most of the atoms from the blue MOT and bridge the large gap between the Doppler cooling regimes of the blue and red transitions [48]. Once the atoms are transferred, the broadband modulation is turned off and the *single-frequency* (SF) red MOT provides final cooling to the few-µK regime, while concurrently raising the atomic density.

Both the blue and red MOTs are formed by three retro-reflected beams, a configuration chosen to simplify the optical setup and reduce laser power requirements compared to six independent beams. The two horizontal beams have a high incidence angle of $\approx 65^\circ$ on the glass cell surface, which leads to a 16% power loss for the reflected beams, that is compensated by refocusing them with a long-focal-distance lens (Thorlabs, Newton, USA, LA1259-AB). The MOTs are characterized using absorption imaging. A resonant 461 nm probe beam is imaged onto a CMOS camera (Basler, Ace acA4024-29um), and a standard sequence of three images (atoms, probe beam, and background) is acquired. The background is subtracted from both the atoms and probe images, and then the ratio of the latter two is used to retrieve a 2D map of the optical column density (OD) profile that, through a calibration, allows the precise determination of the atom number and of the cloud density.

2.5. Optical Tweezer Array and Single-Atom Detection

The optical tweezer array is generated by modulating a high-power 813 nm beam with a pair of orthogonally oriented acousto-optic deflectors (AODs) (AA Opto-Electronic, Orsay, France, DTSX-400-810) [49–53], coupled by a 1 : 1 lens relay in a $4f$ arrangement, as illustrated in Figure 1b. The RF signals that drive the AODs can be actively programmed by an AWG (Spectrum Instrumentation, Grosshansdorf, Germany, M4i.6631-x8). This configuration provides dynamic control over the beam positions and amplitudes, enabling the creation of programmable tweezer patterns with adjustable geometry and site spacing. The modulated light is then tightly focused onto the atomic ensemble using a custom high-numerical-aperture objective (Special Optics, NA = 0.55), mounted on a five-axis positioning stage, producing optical traps with sub-μm waist and suitable depth for single-atom confinement.

The atoms loaded into the tweezers undergo further cooling via narrow-line Sisyphus cooling [34,54,55] on the intercombination transition. To ensure single-atom occupancy, light-assisted collisions (LAC) [23,56–60] are induced, which efficiently remove pairs of atoms from the traps, while preserving single atoms (see Section 3.5). This process yields an average single-site filling fraction of approximately 50%, consistent with the stochastic nature of collisional-blockade loading.

High-fidelity detection of the trapped atoms is achieved using the same high-NA objective employed for tweezer generation [23,61,62]. Atomic fluorescence, collected during resonant orthogonal illumination on the 461 nm transition, is imaged onto a low-noise qCMOS camera (Hamamatsu Photonics, Hamamatsu, Japan, ORCA-Quest). The optical system provides high resolution at the single-site level, while the camera's sensitivity and low background noise enable single-atom detection with a high fidelity exceeding 99.9%. This combination of programmable optical potentials, efficient cooling, controlled collisional loading, and high-fidelity imaging are the key features required to make our experimental setup a robust and scalable platform for quantum simulation and quantum information processing with alkaline-earth atoms.

2.6. Experiment Control System

To guarantee an efficient, flexible and reliable experiment preparation and execution, the entire experimental cycle is controlled through the *Labscript Suite* [63], an open-source Python-based framework specifically designed for atomic-physics experiments. It provides intuitive graphical user interfaces (GUI) and on-line data analysis, with closed-loop feedback and optimization capability. Several devices are natively supported by the Labscript developers (e.g., PulseBlaster boards, IMAQ cameras), while additional hardware support has been contributed by users over time. In our experiment, the currently implemented devices include a custom FPGA timing system [64], based on the Cora Z7 Zynq-7000 System on a Chip, providing through extension boards many TTL and ±10 V analog outputs; Moglabs QRF four channel radio-frequency drivers for AOM/AOD; Basler Ace cameras; Andor iXon Ultra 888 and Hamamatsu ORCA-Quest cameras; and Spectrum Instrumentation M4i AWG boards.

The sequences that control each specific experimental run are written as a single Python script. To streamline sequence development, we created a dedicated library that provides functions for common experimental actions, such as TTL pulses, voltage ramps, or even for entire routines, such as MOT loading or imaging procedures, making the script sequence easy to be read. This library can be simply imported into the script and the execution of each sequence block can be configured via case flags that are set through boolean values in the global parameters section of the *runmanager* GUI. Therefore, from the same interface, users can easily adjust parameters, launch scans, and perform calibrations. Figure 2 displays a typical experimental run, consisting of five blocks corresponding to the three atomic cooling stages, optical trapping in tweezers and imaging. Their respective durations, optical beam intensities, magnetic field gradient, and tweezer potential depth are also shown.

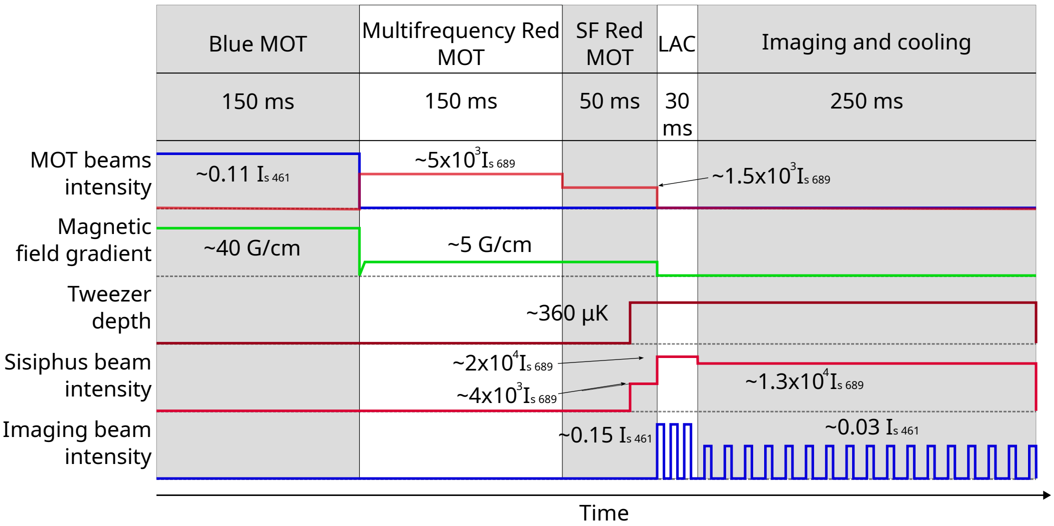

Figure 2. Temporal sequence of the atomic cooling, trapping in tweezers and imaging process. The diagram shows the different experimental stages (Blue MOT, Multifrequency Red MOT, Single Frequency Red MOT, LAC, Imaging and cooling) with their durations, along with the time evolution of the optical beam intensities, magnetic field gradient, and tweezer potential depth.

3. Characterization and Results

3.1. Absorption Imaging Analysis Procedure

The MOTs are characterized using standard absorption imaging and the atom number N_{atoms} is extracted by fitting the absorption profile with a two-dimensional Gaussian (with σ_x^2, σ_y^2 variances), which after integration yields

$$N_{\text{atoms}} = 2\pi\,\sigma_x\sigma_y\,\frac{n_0}{\sigma}, \tag{1}$$

where n_0 is the optical density peak and σ is the atomic resonant absorption cross section.

All absorption images are acquired in time-of-flight (TOF) measurements, where the MOT lasers and magnetic fields are switched off and the atoms then expand freely under gravity. The expansion dynamics of the cloud is determined by its temperature. For a thermal gas far from quantum degeneracy, the velocity distribution follows the Maxwell–Boltzmann statistics [65], giving

$$\tilde{n}(x,y,t) = n_o \exp\left[-\frac{(x-x_0)^2}{2\sigma_x^2(t)} - \frac{(y-y_0)^2}{2\sigma_y^2(t)}\right], \quad \sigma_i^2(t) = \sigma_{0i}^2 + \sigma_v^2 t^2, \tag{2}$$

with $\sigma_v^2 = k_B T/M$, where M is the atomic mass. The cloud widths $\sigma_i(t)$ increase with the expansion time t, and by fitting $\sigma_x(t)$ and $\sigma_y(t)$ we obtain independent estimates of the expansion velocity. Within the experimental uncertainty, we find $\sigma_{v_x}^2 = \sigma_{v_y}^2$, and use their average $\sigma_{avg}(t)$ to extract the temperature.

3.2. Blue Shielded MOT

Under our typical operating conditions, we obtain a blue MOT collecting around 1.25×10^7 atoms at a peak density of $4 \times 10^9\,\mathrm{cm}^{-3}$ over 150 ms, with a temperature of 6.8 mK. Its performance is optimized by scanning key parameters, including the quadrupole magnetic field gradient, the power and detuning of the 3D MOT beams, and the power and detuning of the 2D MOT and Zeeman slower beams. Figure 3a presents a simplified schematic of the electronic level structure of ^{88}Sr, showing the key optical transitions employed during this stage of the experiment.

In Figure 3b, we report the characterization of the dynamics of the blue *shielded* MOT cloud loading with/without the repumping lasers. The presence of the 707 nm repumper (green) triples the number of trapped atoms by preventing optical pumping into the dark metastable $|^3\mathrm{P}_2\rangle$ state. When the 679 nm repumper is also simultaneously applied (red), the loss channel to the dark metastable $|^3\mathrm{P}_0\rangle$ state is also inhibited, which increases the atom number by more than one order of magnitude compared to the case without repumpers (blue). Synergistically, the use of the *shielding* beam yields a $\approx 80\%$ improvement in atom number with respect to the unshielded configuration, as shown in Figure 3c. The spectrum shape is due to the Zeeman splitting of the different m_J Zeeman substates of $|^3\mathrm{P}_1\rangle$ integrated over the MOT extension [46].

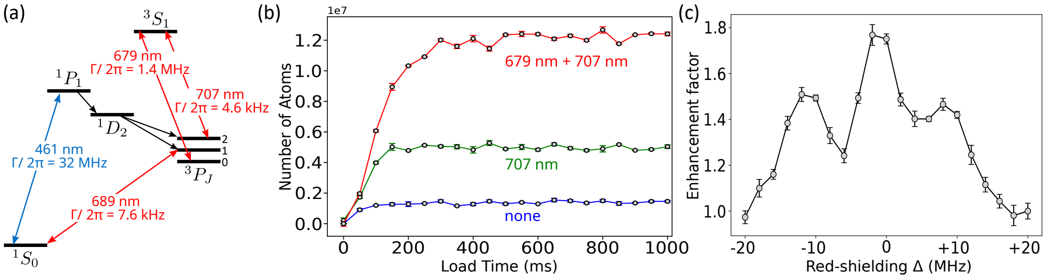

Figure 3. Blue shielded MOT characterization. (**a**) Simplified electronic level structure of ^{88}Sr displaying the transitions of interest. (**b**) Loading curves of the shielded blue MOT for different repumping configurations. The presence of the 707 nm repumper (green) increases the number of trapped atoms by preventing optical pumping into the dark metastable $|^3\mathrm{P}_2\rangle$ state. When the 679 nm repumper is also simultaneously applied (red), the loss channel to the dark metastable $|^3\mathrm{P}_0\rangle$ state is also inhibited, which increases the atom number by more than one order of magnitude compared to the case without any repumper (blue). (**c**) Relative enhancement of the atom number by the red-shielding beam as a function of the frequency detuning from resonance, assuming the far from resonance values as baseline. Error bars in (**b**,**c**) represent standard deviations.

To account for correlations between parameters, such as laser power and detuning Δ, two-dimensional optimization scans (not reported as figures) are performed. Complementarily, we report the saturation parameter $s = I/I_{\mathrm{sat}}$, where I is the peak beam intensity and I_{sat} is the saturation intensity for the addressed transition. Optimal conditions are found for 2D MOT beams with powers of 9.4 mW ($s = 0.11$) and 4.7 mW ($s = 0.055$) at the entrance of the atomic source chamber, detuned by $\Delta_{\mathrm{2D,461}}/2\pi = -0.7\,\Gamma_{^1\mathrm{P}_1}/2\pi = -22\,\mathrm{MHz}$, with saturation intensity $I_{\mathrm{sat,461}} = 42\,\mathrm{mW\,cm^{-2}}$. The Zeeman slower optimal operation power is 40 mW ($s = 0.93$) with a detuning of $\Delta_{\mathrm{Zeeman,461}}/2\pi = -19\,\Gamma_{^1\mathrm{P}_1}/2\pi = -580\,\mathrm{MHz}$. The 3D MOT beams operate optimally at 4.3 mW per beam ($s = 0.1$) with a detuning of $\Delta_{\mathrm{3D,461}}/2\pi = -2\,\Gamma_{^1\mathrm{P}_1}/2\pi = -60\,\mathrm{MHz}$. The quadrupole gradient is set to $50\,\mathrm{G\,cm^{-1}}$, which provides the best compromise between atom number and density. A typical absorption image of the blue shielded MOT is shown in Figure 4a.

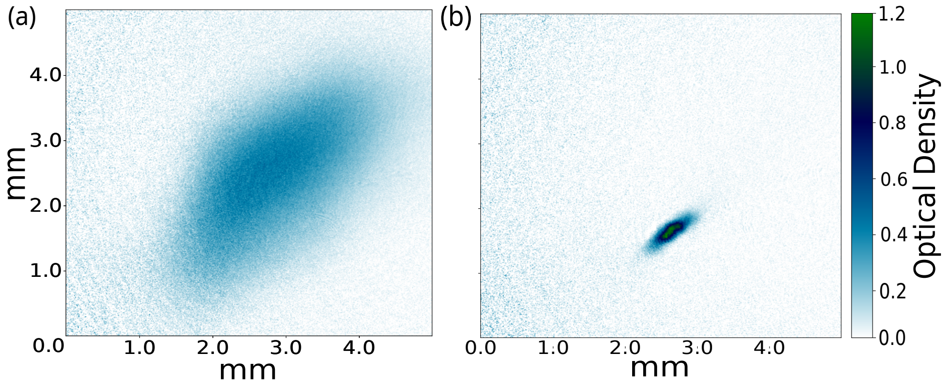

Figure 4. Absorption images of laser-cooled ^{88}Sr clouds: (**a**) a blue shielded MOT with $\sim 1.25 \times 10^7$ atoms at 6.8 mK and (**b**) a single-frequency red MOT with more than 5×10^5 atoms at 5.4 µK. The false-color optical density scale is the same in both absorption images to allow direct visual comparison.

3.3. Multi-Frequency Red MOT

For the intermediate cooling stage, we employ a BB red MOT for 150 ms. To generate a multi-frequency laser beam, we modulate the RF signal driving the AOM that controls the red 3D MOT beams. An AWG (Siglent Technologies, Shenzhen, China, SDG6022X) produces a sinusoidal modulation of the RF carrier with frequency 30 kHz and modulation depth ±2.4 MHz. The Fourier spectrum of this signal consists of a comb of frequency components with 30 kHz spacing, extending over 4.8 MHz. Owing to the double-pass configuration of the AOM, the effective frequency comb in the laser light covers 9.6 MHz. Among the available modulation schemes, the sinusoidal modulation provides the steepest roll-off of sidebands outside the modulation span, ensuring that the comb terminates near the atomic resonance without introducing significant blue-detuned components that could otherwise heat the atoms. Ideally, the comb should be fully red-detuned, extending from few $\Gamma_{^3\mathrm{P}_1}$ below the $^1\mathrm{S}_0 \to {}^3\mathrm{P}_1$ resonance toward lower frequencies. In practice, with our AWG we can adjust the central frequency and total span, which set the effective upper and lower limits of the comb. Immediately after the transfer from the blue MOT, all frequency components contribute to the cooling process. As the atoms decelerate, the Doppler shift decreases and only the less-detuned frequencies remain effective. In principle, the frequency comb could be dynamically narrowed to a single frequency to further cool the atoms. Nevertheless, as we proved, efficient transfer into a single-frequency red MOT is still possible because the saturated linewidth covers the gap between the broadband comb and a narrowband single frequency. Each 3D MOT beam in the BB stage has 4 mW total power distributed over 320 frequency components. For a beam waist of 8 mm and a saturation intensity of $I_{\mathrm{sat},689} = 3\,\mu\mathrm{W\,cm^{-2}}$, we estimate that each component has a saturation parameter of $s \simeq 4.2$, corresponding to a power-broadened linewidth of $\Gamma_s/2\pi = 17\,\mathrm{kHz}$.

During the transfer from the blue to the red MOT, the magnetic field gradient must be rapidly reduced from $50\,\mathrm{G\,cm^{-1}}$ to a few $\mathrm{G\,cm^{-1}}$. This is implemented by switching off the quadrupole coils at the end of the blue 3D MOT stage, together with the blue 3D MOT beams, and then reactivating them at the desired current value. The fast current switch-off circuit enables a decay time of 240(10) µs, leaving the atoms in free fall for just a few hundred microseconds before the current ramps up again. As the gradient increases from 0 to the set value, the trapping region contracts and the cloud is gradually compressed. After testing different final values, we selected a gradient of $5\,\mathrm{G\,cm^{-1}}$, which yields the largest trapped atom number and highest density. A TOF measurement during the broadband stage gives a temperature of $T_{\mathrm{BB}} = 21\,\mu\mathrm{K}$ with approximately 5×10^5 atoms trapped with a peak density of $3.5 \times 10^8\,\mathrm{cm^{-3}}$.

3.4. Single-Frequency Red MOT

The final cooling stage is a SF red MOT that lasts for 50 ms. Efficient transfer from the BB MOT is achieved by starting the SF sequence at a high laser intensity saturation parameter ($s \simeq 200$), which corresponds to a power-broadened linewidth of $\Gamma_s/2\pi = 105\,\mathrm{kHz}$. This broadening bridges effectively the frequency gap between the broadband comb and a narrow single frequency. With this approach, more than 80% of the atoms are transferred from the BB to the SF MOT. Then the power is linearly ramped down by 20%. A TOF expansion yields a final temperature of 5.4 µK, compared to the Doppler limit of 2.4 µK for the broadened linewidth. Importantly, only in this stage we achieve atomic densities above the threshold required for efficient tweezer loading ($n > 3 \times 10^{10}\,\mathrm{cm}^{-3}$, estimated assuming an average of one atom in a tweezer trapping volume). Under optimized conditions, we obtain more than 5×10^5 atoms at a density of $n \simeq 4 \times 10^{10}\,\mathrm{cm}^{-3}$. A typical SF MOT is shown in Figure 4b and has waists $\sigma_x = 50\,\mu\mathrm{m}$ and $\sigma_y = 250\,\mu\mathrm{m}$. To maintain optimal conditions and compensate for the slow linear drift of the ULE cavity used for frequency stabilization ($\sim 12\,\mathrm{kHz/day}$), we perform daily optimization scans of the SF MOT laser frequency and power, typically achieving the best performance at a detuning $\Delta_{3D,689}/2\pi = -100\,\mathrm{kHz}$ and $s \simeq 200$.

3.5. Single Atoms in Optical Tweezers Array

The AOD-generated optical tweezer array is turned on shortly before the end of the red SF MOT and can span a two-dimensional field of view with a lateral size of $\sim 400\,\mu\mathrm{m}$, which is comparable to the atom cloud size. Using the compensation coils, we achieve precise spatial overlap between the MOT and the tweezers array, with a sensitivity of $2\,\mu\mathrm{m/mG\,cm}^{-1}$. Each optical tweezer has a waist of $\sim 1.5\,\mu\mathrm{m}$ and a trap depth of $\sim 360\,\mu\mathrm{K}$, well suited for single-atom trapping.

To achieve single-atom occupancy, we apply a LAC sequence for 30 ms by shining a $\Delta_{\mathrm{LAC},689}/2\pi = -2\,\mathrm{MHz}$ red-detuned 689 nm beam ($s = 2 \times 10^4$) and we speed up the loss process by adding pulsed resonant 461 nm light with a 1 ms duration and 333 Hz repetition rate ($s = 0.15$), as in [21]. As a result, we obtain a single-atom loading probability of $\sim 50\%$ across the array.

Next, to detect the tweezer occupation, fluorescence imaging is performed for 250 ms by pulsing a resonant 461 nm beam (1 ms pulses at 333 Hz repetition rate, $s = 0.03$). During imaging, a $\Delta_{\mathrm{Sis},689}/2\pi = -2.1\,\mathrm{MHz}$ red-detuned 689 nm beam ($s = 1.3 \times 10^4$) is used to implement Sisyphus cooling on the $|^1\mathrm{S}_0\rangle \rightarrow |^3\mathrm{P}_1\rangle$ intercombination line. This cooling stage mitigates photon-scattering-induced heating and enables repeated non-destructive imaging. An image averaged over 100 realizations of a 3 × 3 array of single atoms is shown in the inset of Figure 5(a). The resulting bimodal photon-count distribution collected at the expected atom positions in a region of interest of 3 × 3 pixels (Fig. 5(a)) allows us to discriminate between empty and occupied tweezers. The histogram of the photon distribution is fitted with the sum of two skewed gaussians representing, respectively, the positive detection of an empty site and of a singly occupied one. We define a threshold that determines whether a detected number of counts is attributed to the two situations. The tail of the empty trap distribution that lies beyond the threshold represents the false positive error probability ε_1, while the tail of the occupied trap distribution that lies below the threshold represents the false negative error probability ε_2. The fidelity is calculated as $\mathcal{F} = 1 - (\varepsilon_1 + \varepsilon_2)$ and the threshold value is optimized to maximize $\mathcal{F}$, finding a peak single-atom detection fidelity of $\mathcal{F} = 99.986(6)\%$ (Figure 5b, red data in the inset that focuses on the first points).

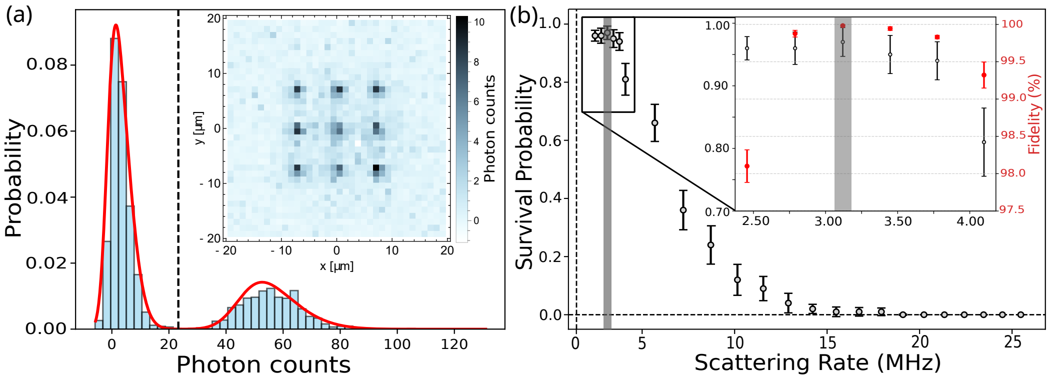

Figure 5. Characterization of single atoms in tweezers through fluorescence detection. (**a**) The histogram of photon counts collected in ROIs centered at the atom positions (averaged over the array) features a bimodal distribution corresponding to empty and occupied traps, that is fitted with the sum of two skewed gaussians (red line); the dashed line at ~ 23 photon counts indicates the threshold value that maximizes the fidelity of true positive single-atom detection. Insert: typical fluorescence image of a 3×3 array of single atoms, obtained by averaging 100 individual acquisitions. (**b**) Trapped atom survival probability and detection fidelity $\mathcal{F}$ (in red in the inset that focuses on the first points) as a function of the probe beam scattering rate. All data is taken with a fixed imaging duration of 150 ms, chosen to ensure that for every scattering rate the detected signal was sufficiently strong to allow accurate evaluation of both quantities. The shaded region indicates the optimal scattering-rate value. Error bars represent standard deviations calculated with the bootstrapping method [66].

Furthermore, the implementation of Sisyphus cooling ensures a survival probability of 97(2)% during imaging, confirming the robustness of the protocol (Figure 5b, black data). The survival probability is obtained from two consecutive images as the ratio between the number of populated tweezers in the second image over those detected in the first, providing a direct measure of atom loss during imaging.

We characterize the temperature of the trapped atoms using a release-and-recapture measurement (Figure 6a) [67,68]. In this technique, the trapping potential is briefly switched off for a variable release time, after which the tweezers are restored and the probability of recapturing the atom is measured by acquiring a second image. As expected, the recapture probability decreases with longer release times, since atoms with higher kinetic energy are more likely to escape. The experimental data is compared to a Monte-Carlo simulation of atomic dynamics in the tweezer potential, from which we extract the atomic temperature, and we find the best agreement at a temperature of 12.92(5) μK.

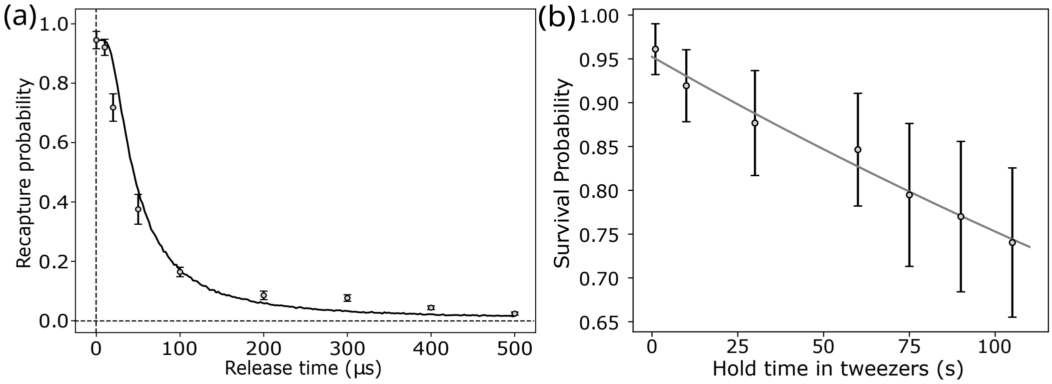

Figure 6. (**a**) Recapture probability as a function of release time during a release-and-recapture measurement, which provides an atom temperature of 12.92(5) µK through the comparison with Monte-Carlo simulations (solid line). (**b**) Estimation of the vacuum-limited lifetime by fitting the atom survival probability as a function of the tweezer hold time with an exponential function (solid line). The fitted lifetime is 425(25) s. Error bars in (**a**,**b**) represent standard deviations calculated with the bootstrapping method [66].

Finally, to assess the background vacuum conditions, we measure the lifetime of atoms trapped in the tweezers (Figure 6b) by holding them for a variable time, up to several minutes, after which we acquire a second fluorescence image from which we extract the survival probability. The population decay is fitted to an exponential law, from which we extract a vacuum-limited lifetime of 425(25) s. This long lifetime indicates very good ultra-high vacuum conditions in the experimental chamber and demonstrates that background gas collisions are not a limiting factor for the experiments reported in this work.

4. Conclusions

We have developed and characterized a neutral-atom quantum simulation platform based on individually trapped ^{88}Sr atoms in optical tweezers. A key component of the system is a two-stage MOT operating on the $|^1\mathrm{S}_0\rangle \rightarrow |^1\mathrm{P}_1\rangle$ transition at 461 nm and on the narrow $|^1\mathrm{S}_0\rangle \rightarrow |^3\mathrm{P}_1\rangle$ intercombination line at 689 nm. Using a blue shielded MOT scheme allows us to enhance the atom number by up to 80%. Sequential broadband and single-frequency cooling stages yield atomic samples at temperatures of 5.4 µK and densities $4 \times 10^{10}\,\mathrm{cm}^{-3}$, providing ideal conditions for tweezer loading.

The achieved single-atom detection fidelity of $\mathcal{F} = 99.986(6)\%$ and survival probability of $97(2)\%$ are comparable to those reported in similar Yb and Sr tweezer experiments [21,23,24,26], while the measured temperature of $\sim 13\,\mu\mathrm{K}$ in the optical tweezers confirms the efficiency of our in-tweezer cooling scheme. Furthermore, the observed vacuum-limited lifetime exceeding seven minutes is on par with, or better than, similar optical tweezer systems [13,60], highlighting the quality of the ultra-high-vacuum environment achieved in our setup. These performance indicators demonstrate that our apparatus provides the necessary conditions for high-fidelity single-atom preparation and readout, laying the groundwork for the implementation of advanced programmable Rydberg-based quantum simulators with alkaline-earth Sr neutral atoms.

Author Contributions: Conceptualization and methodology, V.G. (Vladislav Gavryusev), J.C., G.C. and L.F.; software, A.F.; validation, V.G. (Veronica Giardini), A.F. and V.G. (Vladislav Gavryusev); formal analysis, A.F. and V.G. (Veronica Giardini); investigation, V.G. (Veronica Giardini), L.G., A.F. and S.S.; data curation and visualization, V.G. (Veronica Giardini) and A.F.; writing—original draft preparation, V.G. (Veronica Giardini), A.F., L.G. and V.G. (Vladislav Gavryusev); writing—review and editing, all authors; supervision, project administration, resources and funding acquisition, V.G.

(Vladislav Gavryusev), M.I., J.C., G.C. and L.F.. All authors have read and agreed to the published version of the manuscript.

Funding: This project has received funding from Consiglio Nazionale delle Ricerche (CNR) PASQUA Infrastructure, QuantERA ERA-NET Cofund in Quantum Technologies project MENTA, from the Italian Ministry of Education and Research (MUR) PRIN 2022SJCKAH "HIGHEST", and, in the context of the National Recovery and Resilience Plan and Next Generation EU, from M4C2 investment 1.2 project MicroSpinEnergy (Vladislav Gavryusev).

Data Availability Statement: The original contributions presented in this study are included in the article. The raw data supporting the conclusions of this article will be made available by the authors on request. Further inquiries can be directed to the corresponding author.

Acknowledgments: We acknowledge insightful discussions and collaboration on the initial planning steps with Francesco Scazza. We thank the mechanical and electronic workshops of LENS and of the Physics and Astronomy Department for their support.

Conflicts of Interest: The authors declare no conflict of interest.

References

1. Zhang, X.; Ye, J. Precision measurement and frequency metrology with ultracold atoms. *National Science Review* **2016**, *3*, 189–200, [https://academic.oup.com/nsr/article-pdf/3/2/189/31565570/nww013.pdf]. https://doi.org/10.1093/nsr/nww013.
2. Bernien, H.; Schwartz, S.; Keesling, A.; Levine, H.; Omran, A.; Pichler, H.; Choi, S.; Zibrov, A.S.; Endres, M.; Greiner, M.; et al. Probing many-body dynamics on a 51-atom quantum simulator. *Nature* **2017**, *551*, 579–584, [1707.04344]. https://doi.org/10.1038/nature24622.
3. Browaeys, A.; Lahaye, T. Many-body physics with individually controlled Rydberg atoms. *Nature Physics* **2020**, *16*, 132–142. https://doi.org/10.1038/s41567-019-0733-z.
4. Yago Malo, J.; Lepori, L.; Gentini, L.; Chiofalo, M.L.M. Atomic Quantum Technologies for Quantum Matter and Fundamental Physics Applications. *Technologies* **2024**, *12*, 64. https://doi.org/10.3390/technologies12050064.
5. Sales Rodriguez, P.; Robinson, J.M.; Jepsen, P.N.; He, Z.; Duckering, C.; Zhao, C.; Wu, K.H.; Campo, J.; Bagnall, K.; Kwon, M.; et al. Experimental demonstration of logical magic state distillation. *Nature* **2025**, *645*, 620–625, [arXiv:quant-ph/2412.15165]. https://doi.org/10.1038/s41586-025-09367-3.
6. Chiu, N.C.; Trapp, E.C.; Guo, J.; Abobeih, M.H.; Stewart, L.M.; Hollerith, S.; StrogaNov, P.L.; Kalinowski, M.; Geim, A.A.; Evered, S.J.; et al. Continuous operation of a coherent 3,000-qubit system. *Nature* **2025**, *646*, 1075–1080, [arXiv:quant-ph/2506.20660]. https://doi.org/10.1038/s41586-025-09596-6.
7. Zhou, H.; Zhao, C.; Cain, M.; Bluvstein, D.; Maskara, N.; Duckering, C.; Hu, H.Y.; Wang, S.T.; Kubica, A.; Lukin, M.D. Low-overhead transversal fault tolerance for universal quantum computation. *Nature* **2025**, *646*, 303–308, [arXiv:quant-ph/2406.17653]. https://doi.org/10.1038/s41586-025-09543-5.
8. Wolswijk, L.; Cavicchioli, L.; Vinelli, G.; Chiarotti, M.; Donati, L.; Frometa Fernandez, M.; Hernández Rajkov, D.; Mancini, C.; Vezio, P.; Zhou, T.; et al. Trapping, manipulating and probing ultracold atoms: a quantum technologies tutorial. *arXiv e-prints* **2025**, p. arXiv:2510.20790, [arXiv:cond-mat.quant-gas/2510.20790].
9. Saffman, M.; Walker, T.G.; Mølmer, K. Quantum information with Rydberg atoms. *Reviews of Modern Physics* **2010**, *82*, 2313–2363. https://doi.org/10.1103/RevModPhys.82.2313.
10. Levine, H.; Keesling, A.; Semeghini, G.; Omran, A.; Wang, T.T.; Ebadi, S.; Bernien, H.; Greiner, M.; Vuletić, V.; Pichler, H.; et al. Parallel Implementation of High-Fidelity Multiqubit Gates with Neutral Atoms. *Physical Review Letters* **2019**, *123*, 170503. https://doi.org/10.1103/PhysRevLett.123.170503.
11. Scholl, P.; Williams, H.J.; Bornet, G.; Wallner, F.; Barredo, D.; Henriet, L.; Signoles, A.; Hainaut, C.; Franz, T.; Geier, S.; et al. Microwave Engineering of Programmable XXZ Hamiltonians in Arrays of Rydberg Atoms. *PRX Quantum* **2022**, *3*, 020303, [arXiv:quant-ph/2107.14459]. https://doi.org/10.1103/PRXQuantum.3.020303.
12. Bornet, G.; Emperauger, G.; Chen, C.; Ye, B.; Block, M.; Bintz, M.; Boyd, J.A.; Barredo, D.; Comparin, T.; Mezzacapo, F.; et al. Scalable spin squeezing in a dipolar Rydberg atom array. *Nature* **2023**, *621*, 728–733, [arXiv:quant-ph/2303.08053]. https://doi.org/10.1038/s41586-023-06414-9.
13. Madjarov, I.S.; Covey, J.P.; Shaw, A.L.; Choi, J.; Kale, A.; Cooper, A.; Pichler, H.; Schkolnik, V.; Williams, J.R.; Endres, M. High-fidelity entanglement and detection of alkaline-earth Rydberg atoms. *Nature Physics* **2020**, *16*, 857–861. https://doi.org/10.1038/s41567-020-0903-z.

14. Graham, T.M.; Song, Y.; Scott, J.; Poole, C.; Phuttitarn, L.; Jooya, K.; Eichler, P.; Jiang, X.; Marra, A.; Grinkemeyer, B.; et al. Multi-qubit entanglement and algorithms on a neutral-atom quantum computer. *Nature* **2022**, *604*, 457–462, [arXiv:quant-ph/2112.14589]. https://doi.org/10.1038/s41586-022-04603-6.
15. Bloom, B.J.; Nicholson, T.L.; Williams, J.R.; Campbell, S.L.; Bishof, M.; Zhang, X.; Zhang, W.; Bromley, S.L.; Ye, J. An optical lattice clock with accuracy and stability at the 10^{-18} level. *Nature* **2014**, *506*, 71–75. https://doi.org/10.1038/nature12941.
16. Finkelstein, R.; Tsai, R.B.S.; Sun, X.; Scholl, P.; Direkci, S.; Gefen, T.; Choi, J.; Shaw, A.L.; Endres, M. Universal quantum operations and ancilla-based read-out for tweezer clocks. *Nature* **2024**, *634*, 321–327, [arXiv:quant-ph/2402.16220]. https://doi.org/10.1038/s41586-024-08005-8.
17. Ye, J.; Kimble, H.J.; Katori, H. Quantum State Engineering and Precision Metrology Using State-Insensitive Light Traps. *Science* **2008**, *320*, 1734–1738. https://doi.org/10.1126/science.1148259.
18. Fukuhara, T.; Takasu, Y.; Kumakura, M.; Takahashi, Y. Degenerate Fermi Gases of Ytterbium. *Physical Review Letters* **2007**, *98*, 030401. https://doi.org/10.1103/PhysRevLett.98.030401.
19. Shaw, A.L.; Scholl, P.; Finkelstein, R.; Tsai, R.B.S.; Choi, J.; Endres, M. Erasure cooling, control, and hyperentanglement of motion in optical tweezers. *Science* **2025**, *388*, 845–849, [arXiv:quant-ph/https://www.science.org/doi/pdf/10.1126/science.adn2618]. https://doi.org/10.1126/science.adn2618.
20. Daley, A.J. Quantum computing and quantum simulation with group-II atoms. *Quantum Information Processing* **2011**, *10*, 865. https://doi.org/10.1007/s11128-011-0293-3.
21. Norcia, M.A.; Young, A.W.; Kaufman, A.M. Microscopic Control and Detection of Ultracold Strontium in Optical-Tweezer Arrays. *Physical Review X* **2018**, *8*, 041054. https://doi.org/10.1103/PhysRevX.8.041054.
22. Nicholson, T.; Campbell, S.; Hutson, R.; Marti, G.; Bloom, B.; McNally, R.; Zhang, W.; Barrett, M.; Safronova, M.; Strouse, G.; et al. Systematic evaluation of an atomic clock at 2×10^{-18} total uncertainty. *Nature Communications* **2015**, *6*, 6896.
23. Cooper, A.; Covey, J.P.; Madjarov, I.S.; Porsev, S.G.; Safronova, M.S.; Endres, M. Alkaline-Earth Atoms in Optical Tweezers. *Physical Review X* **2018**, *8*, 041055. https://doi.org/10.1103/PhysRevX.8.041055.
24. Saskin, S.; Wilson, J.T.; Grinkemeyer, B.; Thompson, J.D. Narrow-Line Cooling and Imaging of Ytterbium Atoms in an Optical Tweezer Array. *Physical Review Letters* **2019**, *122*, 143002. https://doi.org/10.1103/PhysRevLett.122.143002.
25. Wu, Y.; Kolkowitz, S.; Puri, S.; Thompson, J.D. Erasure conversion for fault-tolerant quantum computing in alkaline earth Rydberg atom arrays. *Nature Communications* **2022**, *13*, 4657, [arXiv:quant-ph/2201.03540]. https://doi.org/10.1038/s41467-022-32094-6.
26. Wilson, J.T.; Saskin, S.; Meng, Y.; Ma, S.; Dilip, R.; Burgers, A.P.; Thompson, J.D. Trapping Alkaline Earth Rydberg Atoms Optical Tweezer Arrays. *Physical Review Letters* **2022**, *128*, 033201, [arXiv:quant-ph/1912.08754]. https://doi.org/10.1103/PhysRevLett.128.033201.
27. Gavryusev, V.; Ferreira-Cao, M.; Kekić, A.; Zürn, G.; Signoles, A. Interaction Enhanced Imaging of Rydberg P states. *The European Physical Journal Special Topics* **2016**, *225*, 2863–2889, [arXiv:physics.atom-ph/1602.04143]. https://doi.org/10.1140/epjst/e2015-50339-8.
28. Gavryusev, V.; Signoles, A.; Ferreira-Cao, M.; Zürn, G.; Hofmann, C.S.; Günter, G.; Schempp, H.; de Saint-Vincent, M.R.; Whitlock, S.; Weidemüller, M. Density matrix reconstruction of three-level atoms via Rydberg electromagnetically induced transparency. *Journal of Physics B: Atomic, Molecular and Optical Physics* **2016**, *49*, 164002, [arXiv:physics.atom-ph/1602.07728].
29. Ferreira-Cao, M.; Gavryusev, V.; Franz, T.; Alves, R.F.; Signoles, A.; Zuern, G.; Weidemüller, M. Depletion imaging of Rydberg atoms in cold atomic gases. *Journal of Physics B: Atomic, Molecular and Optical Physics* **2020**, *53*, 084004, [arXiv:physics.atom-ph/1911.06397]. https://doi.org/10.1088/1361-6455/ab7427.
30. Morandi, O.; Nicoletti, S.; Gavryusev, V.; Fallani, L. Optimal control in phase space applied to minimal-time transfer of thermal atoms in optical traps. *Physical Review A* **2025**, *111*, 063312, [arXiv:quant-ph/2501.10494]. https://doi.org/10.1103/d857-7cwr.
31. Gavryusev, V.; Guariento, L.; Giardini, V.; Fantini, A.; Storm, S.; Catani, J.; Inguscio, M.; Fallani, L.; Cappellini, G. A New Programmable Quantum Simulator with Strontium Rydberg Atoms in Optical Tweezer Arrays. In Proceedings of the Quantum 2.0 Conference and Exhibition. Optica Publishing Group, 2024, p. QTh2A.2.
32. Guariento, L. A new setup for single Strontium atoms in Optical Tweezers. PhD thesis, PhD degree in Quantum Technologies, 2025.
33. Covey, J.P.; Madjarov, I.S.; Cooper, A.; Endres, M. 2000-Times Repeated Imaging of Strontium Atoms in Clock-Magic Tweezer Arrays. *Physical Review Letters* **2019**, *122*, 173201. https://doi.org/10.1103/PhysRevLett.122.173201.
34. Urech, A.; Knottnerus, I.H.A.; Spreeuw, R.J.C.; Schreck, F. Narrow-line imaging of single strontium atoms in shallow optical tweezers. *Physical Review Research* **2022**, *4*, 023245. https://doi.org/10.1103/PhysRevResearch.4.023245.
35. Young, A.W.; Eckner, W.J.; Milner, W.R.; Kedar, D.; Norcia, M.A.; Oelker, E.; Schine, N.; Ye, J.; Kaufman, A.M. Half-minute-scale atomic coherence and high relative stability in a tweezer clock. *Nature* **2020**, *588*, 408–413. https://doi.org/10.1038/s41586-020-3009-y.

36. Origlia, S.; Pramod, M.S.; Schiller, S.; Singh, Y.; Bongs, K.; Schwarz, R.; Al-Masoudi, A.; Dörscher, S.; Herbers, S.; Häfner, S.; et al. Towards an optical clock for space: Compact, high-performance optical lattice clock based on bosonic atoms. *Physical Review A* **2018**, *98*, 053443. https://doi.org/10.1103/PhysRevA.98.053443.
37. Baillard, X.; Fouché, M.; Targat, R.L.; Westergaard, P.G.; Lecallier, A.; Coq, Y.L.; Rovera, G.D.; Bize, S.; Lemonde, P. Accuracy evaluation of an optical lattice clock with bosonic atoms. *Optics Letters* **2007**, *32*, 1812–1814. https://doi.org/10.1364/OL.32.001812.
38. Qiao, C.; Tan, C.; Siegl, J.; Hu, F.; Niu, Z.; Jiang, Y.; Weidemüller, M.; Zhu, B. Rydberg blockade in an ultracold strontium gas revealed by two-photon excitation dynamics. *Physical Review A* **2021**, *103*, 063313, [arXiv:physics.atom-ph/2103.04528]. https://doi.org/10.1103/PhysRevA.103.063313.
39. Sorrentino, F.; Ferrari, G.; Poli, N.; Drullinger, R.; Tino, G.M. Laser Cooling And Trapping Of Atomic Strontium For Ultracold Atoms Physics, High-Precision Spectroscopy And Quantum Sensors. *Modern Physics Letters B* **2006**, *20*, 1287–1320, [Https://Doi.Org/10.1142/S0217984906011682]. https://doi.org/10.1142/S0217984906011682.
40. Norcia, M.A.; Cline, J.R.K.; Bartolotta, J.P.; Holland, M.J.; Thompson, J.K. Narrow-line laser cooling by adiabatic transfer. *New Journal of Physics* **2018**, *20*, 023021. https://doi.org/10.1088/1367-2630/aaa950.
41. Snigirev, S.; Park, A.J.; Heinz, A.; Bloch, I.; Blatt, S. Fast and dense magneto-optical traps for strontium. *Physical Review A* **2019**, *99*, 063421. https://doi.org/10.1103/PhysRevA.99.063421.
42. Wen, K.; Chen, H.; Yan, X.; Ren, Z.; He, C.; Hajiyev, E.; Wong, P.T.F.; Jo, G.B. Apparatus for producing single strontium atoms in an optical tweezer array. *Chinese Physics B* **2024**, *33*, 120703, [arXiv:physics.app-ph/2409.05361]. https://doi.org/10.1088/1674-1056/ad84d0.
43. Shao-Kai, W.; Qiang, W.; Yi-Ge, L.; Min-Ming, W.; Bai-Ke, L.; Er-Jun, Z.; Tian-Chu, L.; Zhan-Jun, F. Cooling and Trapping 88Sr Atoms with 461 nm Laser. *Chinese Physics Letters* **2009**, *26*, 093202. https://doi.org/10.1088/0256-307X/26/9/093202.
44. Hu, F.; Nosske, I.; Couturier, L.; Tan, C.; Qiao, C.; Chen, P.; Jiang, Y.H.; Zhu, B.; Weidemüller, M. Analyzing a single-laser repumping scheme for efficient loading of a strontium magneto-optical trap. *Physical Review A* **2019**, *99*, 033422. https://doi.org/10.1103/PhysRevA.99.033422.
45. Patel, K.; Gakkhar, P.; Biswas, K.; Sagar Maurya, S.; Dutta, P.; Lal, V.; Mani, B.K.; Rapol, U.D. Spectroscopy of the $5s5p^3P_0 \rightarrow 5s5d^3D_1$ transition of strontium using laser cooled atoms. *Journal of Physics B: Atomic, Molecular and Optical Physics* **2024**, *57*, 105501. https://doi.org/10.1088/1361-6455/ad3bff.
46. Höschele, J.; Buob, S.; Rubio-Abadal, A.; Makhalov, V.; Tarruell, L. Atom-Number Enhancement by Shielding Atoms From Losses in Strontium Magneto-Optical Traps. *Physical Review Applied* **2023**, *19*, 064011, [arXiv:cond-mat.quant-gas/2302.02992]. https://doi.org/10.1103/PhysRevApplied.19.064011.
47. Poli, N.; Schioppo, M.; Vogt, S.; Falke, S.; Sterr, U.; Lisdat, C.; Tino, G. A transportable strontium optical lattice clock. *Applied Physics B* **2014**, *117*, 1107–1116. https://doi.org/10.1007/s00340-014-5932-9.
48. Phalen, D.J.; Young, C.C.; Yi, S.; Pu, H. Multidimensional laser cooling of broad- and narrow-line 0 ↔ 1 dipole transitions. *Physical Review A* **2005**, *72*, 033406. https://doi.org/10.1103/PhysRevA.72.033406.
49. Labuhn, H.; Ravets, S.; Barredo, D.; Béguin, L.; Nogrette, F.; Lahaye, T.; Browaeys, A. Single-atom addressing in microtraps for quantum-state engineering using Rydberg atoms. *Physical Review A* **2014**, *90*, 023415. https://doi.org/10.1103/PhysRevA.90.023415.
50. Nogrette, F.; Labuhn, H.; Ravets, S.; Barredo, D.; Béguin, L.; Vernier, A.; Lahaye, T.; Browaeys, A. Single-Atom Trapping in Holographic 2D Arrays of Microtraps with Arbitrary Geometries. *Physical Review X* **2014**, *4*, 021034. https://doi.org/10.1103/PhysRevX.4.021034.
51. Barredo, D.; de Léséleuc, S.; Lienhard, V.; Lahaye, T.; Browaeys, A. An atom-by-atom assembler of defect-free arbitrary two-dimensional atomic arrays. *Science* **2016**, *354*, 1021–1023, [arXiv:quant-ph/http://science.sciencemag.org/content/354/6315/1021.full.pdf]. https://doi.org/10.1126/science.aah3778.
52. Ricci, P.; Marchetti, M.; Sorelli, M.; Turrini, L.; Resta, F.; Gavryusev, V.; de Vito, G.; Sancataldo, G.; Vanzi, F.; Silvestri, L.; et al. Power-effective scanning with AODs for 3D optogenic applications. *Journal of Biophotonics* **2022**, *15*, e202100256, [https://onlinelibrary.wiley.com/doi/pdf/10.1002/jbio.202100256]. e202100256 jbio.202100256.R2, https://doi.org/10.1002/jbio.202100256.
53. Ricci, P.; Sancataldo, G.; Gavryusev, V.; Pavone, F.S.; Saggau, P.; Duocastella, M. Acousto-optic deflectors in experimental neuroscience: overview of theory and applications. *Journal of Physics: Photonics* **2024**, *6*, 022001. https://doi.org/10.1088/2515-7647/ad2e0d.
54. Dalibard, J.; Cohen-Tannoudji, C. Laser cooling below the Doppler limit by polarization gradients: simple theoretical models. *Journal of the Optical Society of America B* **1989**, *6*, 2023–2045. https://doi.org/10.1364/JOSAB.6.002023.
55. Hölzl, C.; Götzelmann, A.; Wirth, M.; Safronova, M.S.; Weber, S.; Meinert, F. Motional ground-state cooling of single atoms in state-dependent optical tweezers. *Physical Review Research* **2023**, *5*, 033093. https://doi.org/10.1103/PhysRevResearch.5.033093.

56. Sompet, P.; Carpentier, A.V.; Fung, Y.H.; McGovern, M.; Andersen, M.F. Dynamics of two atoms undergoing light-assisted collisions in an optical microtrap. *Physical Review A* **2013**, *88*, 051401. https://doi.org/10.1103/PhysRevA.88.051401.
57. Labuhn, H. Creating arbitrary 2D arrays of single atoms for the simulation of spin systems with Rydberg states. *The European Physical Journal Special Topics* **2016**, *225*, 2817–2838. https://doi.org/10.1140/epjst/e2015-50336-5.
58. Fung, Y.H.; Sompet, P.; Andersen, M.F. Single Atoms Preparation Using Light-Assisted Collisions. *Technologies* **2016**, *4*. https://doi.org/10.3390/technologies4010004.
59. Brown, M.O.; Thiele, T.; Kiehl, C.; Hsu, T.W.; Regal, C.A. Gray-Molasses Optical-Tweezer Loading: Controlling Collisions for Scaling Atom-Array Assembly. *Physical Review X* **2019**, *9*, 011057. https://doi.org/10.1103/PhysRevX.9.011057.
60. Jenkins, A.; Lis, J.W.; Senoo, A.; McGrew, W.F.; Kaufman, A.M. Ytterbium Nuclear-Spin Qubits in an Optical Tweezer Array. *Physical Review X* **2022**, *12*, 021027, [arXiv:physics.atom-ph/2112.06732]. https://doi.org/10.1103/PhysRevX.12.021027.
61. Endres, M.; Bernien, H.; Keesling, A.; Levine, H.; Anschuetz, E.R.; Krajenbrink, A.; Senko, C.; Vuletić, V.; Greiner, M.; Lukin, M.D. Atom-by-atom assembly of defect-free one-dimensional cold atom arrays. *Science* **2016**, *354*, 1024–1027, [arXiv:quant-ph/http://science.sciencemag.org/content/354/6315/1024.full.pdf]. https://doi.org/10.1126/science.aah3752.
62. Tao, R.; Ammenwerth, M.; Gyger, F.; Bloch, I.; Zeiher, J. High-Fidelity Detection of Large-Scale Atom Arrays in an Optical Lattice. *Physical Review Letters* **2024**, *133*, 013401, [arXiv:physics.atom-ph/2309.04717]. https://doi.org/10.1103/PhysRevLett.133.013401.
63. Starkey, P.T.; Billington, C.J.; Johnstone, S.P.; Jasperse, M.; Helmerson, K.; Turner, L.D.; Anderson, R.P. A scripted control system for autonomous hardware-timed experiments. *Review of Scientific Instruments* **2013**, *84*, 085111. https://doi.org/http://dx.doi.org/10.1063/1.4817213.
64. Trenkwalder, A.; Zaccanti, M.; Poli, N. A flexible system-on-a-chip control hardware for atomic, molecular, and optical physics experiments. *Review of Scientific Instruments* **2021**, *92*, 105103, [arXiv:physics.atom-ph/https://doi.org/10.1063/5.0058986]. https://doi.org/10.1063/5.0058986.
65. Metcalf, H.; van der Straten, P. *Laser Cooling and Trapping*; Springer: New York, 1999.
66. Efron, B.; Tibshirani, R. *An Introduction to the Bootstrap*; Chapman & Hall/CRC Monographs on Statistics & Applied Probability, Taylor & Francis, 1993.
67. Tuchendler, C.; Lance, A.M.; Browaeys, A.; Sortais, Y.R.P.; Grangier, P. Energy distribution and cooling of a single atom in an optical tweezer. *Physical Review A* **2008**, *78*, 033425. https://doi.org/10.1103/PhysRevA.78.033425.
68. Muzi Falconi, A.; Panza, R.; Sbernardori, S.; Forti, R.; Klemt, R.; Abdel Karim, O.; Marinelli, M.; Scazza, F. Microsecond-Scale High-Survival and Number-Resolved Detection of Ytterbium Atom Arrays. *Phys. Rev. Lett.* **2025**, *135*, 203402, [arXiv:cond-mat.quant-gas/2507.01011]. https://doi.org/10.1103/n3bg-7yw7.